

On the dynamics of photo-electrons from C_{60}

C.-Z. Gao^{1,2}, P. Wopperer^{1,2}, P. M. Dinh^{1,2}, E. Surraud^{1,2},
and P.-G. Reinhard³

¹ Université de Toulouse; UPS; Laboratoire de Physique Théorique, IRSAMC;
F-31062 Toulouse Cedex, France

² CNRS; UMR5152; F-31062 Toulouse Cedex, France

³ Institut für Theoretische Physik, Universität Erlangen, Staudtstraße 7,
D-91058 Erlangen, Germany

E-mail: dinh@irsamc.ups-tlse.fr

Abstract. We explore photo-electron spectra (PES) and photo-electron angular distributions (PAD) of C_{60} with time-dependent density functional theory (TDDFT) in real time. To simulate experiments in gas phase, we consider isotropic ensembles of cluster orientations and perform orientation averaging of the TDDFT calculations. First, we investigate ionization properties of C_{60} by one-photon processes in the range of VUV energies. The PES map the energies of the occupied single-particle states, while the weights of the peaks in PES are given by the depletion of the corresponding level. The different influences can be disentangled by looking at PES from slightly different photon frequencies. PAD in the one-photon regime can be characterized by one parameter, the anisotropy. This single parameter unfolds worthwhile information when investigating the frequency and state dependences. We also discuss the case of multi-photon ionization induced by strong infrared laser pulses in C_{60} . In agreement with measurements, we find that the PES show a regular comb of peaks separated by the photon energy. Our calculations reveal that this happens because only very few occupied states of C_{60} near the ionization threshold contribute to emission and that these few states happen to cooperate filling the same peaks. The PAD show a steady increase of anisotropy with increasing photon order.

PACS numbers: 33.60.-q, 33.60.Fy, 33.90.+h, 36.40.Vz, 61.46.Bc, 61.48.+c

Submitted to: *J. Phys. B: At. Mol. Opt. Phys.*

1. Introduction

Early investigations of clusters concentrated on structure and optical response [1, 2, 3, 4, 5]. Steady progress of laser physics and experimental analysis has given access to more detailed measurements as photo-electron spectroscopy (PES) [6], photo-electron angular distribution (PAD) [7], and in combination as PES/PAD, often represented also as Velocity Map Imaging (VMI) [8]. These techniques have been taken up intensely in cluster physics delivering a richer information on the system than the mere ground state single electron density of states [9], see e.g. [10]. The more recent investigations can address various dynamical regimes ranging from linear to nonlinear domain by variations of the laser properties (i.e., intensity, duration, and frequency). The much celebrated fullerene C_{60} , which could be regarded as one of archetypical clusters appearing between small molecules and bulk (solid) materials, has been at the core of numerous investigations since several years. Studies on C_{60} show the same development as for clusters in general. They started out with considerations on existence, structure and optical response [11, 12, 13, 14]. First studies on PES came up also rather early [15, 16, 17]. More recently, a great manifold of precision measurements of PES and/or PAD have been performed, exploring several dynamical ranges, see e.g. [9, 18, 19, 20, 21, 22, 23].

The development of theory is meanwhile parallel to the advance of measurements. Among the great variety of models, the best compromise between expense and detailed description is achieved by Density Functional Theory (DFT) for the electrons, coupled to the carbon ions by pseudopotentials. This was already used for early investigations of structure [24] and optical response [25]. Recently, anisotropy parameters (characterizing the PAD) have been extracted by using explicit ions and eigenfunctions of the scattering matrix in the framework of static DFT wave functions, see e.g. [26, 27, 28]. Similar calculations have also been performed by employing Linearized Time-Dependent DFT (L-TDDFT), in which free plane waves for the outgoing wave functions are considered in the calculation of the anisotropy parameter β_2 , for various laser frequencies [23]. However, free plane waves might constitute an oversimplification which can significantly impact β_2 , see discussion in Section 5.3.2 and [29]. Other calculations of photo-ionization cross-sections based on L-TDDFT also exist but using a spherical hollow shell jellium background instead of an explicit ionic structure [21, 30, 31]. The jellium approximation has also been used in [32, 33, 34] to calculate cross-sections, but at the level of classical electrodynamics and hydrodynamics. Unfortunately, the jellium approximation suffers from intrinsic limitations : It cannot reproduce the electronic shell closure at $N_{el} = 240$ where it should be and it yields a wrong sequence of single-particle (s.p.) levels. As discussed in our previous works on Na clusters in the one-photon regime, PES, PAD and anisotropy parameters furthermore significantly differ when explicit ions are used instead of a jellium background [35, 36]. This is particularly surprising as Na clusters possess a much better metallic character than the partly covalent C_{60} : the jellium model should therefore work better in Na clusters than in C_{60} . We thus see as compulsory to use an explicit ionic structure of C_{60} (without adjustable parameters) for a quantitative description of PES and PAD, especially for a direct comparison with experimental data.

The aim of this paper is thus to present in detail a model providing a fully fledged microscopic theoretical description of C_{60} using methods of Time-Dependent DFT (TDDFT) in real time and real space, extensively applied and tested previously

in metal cluster dynamics [35, 37, 38, 39]. We will mainly address electronic emission from one-photon processes induced by VUV pulses, but we will also have a look at strong infrared pulses and subsequent multi-photon processes. Where possible, we shall perform comparison with available experiments.

The paper is outlined as follows: Section 2 briefly introduces the theoretical framework. Section 3 discusses electronic and ionic structure of C_{60} and presents results on basic ground-state properties, particularly those which are crucial for a proper description of ionization processes, such as Ionization Potential (IP) and level degeneracies. Section 4 is devoted to the optical absorption spectrum. Section 5 embraces all results on PES/PAD from excitation by photon pulses in the monophoton regime. In this context, we also explain our procedure for calculation of PAD and PES of an ensemble of randomly oriented clusters. Section 6 briefly explores the multiphoton regime. Section 7 finally completes the paper with a summary.

2. Theoretical framework

2.1. On the formalism

The method used here, namely TDDFT in real time and real space coupled to a classical description of ions via pseudopotentials, is standard and has been presented in detail in several papers and books, see e.g. [40, 41]. We shall thus only outline the specificities of the present investigation. We refer the reader to [40] for technical details.

The C_{60} cluster is described in terms of 240 active valence electrons. The coupling to the 60 carbon ions (one C nucleus with 2 core electrons each) is treated by non-local pseudopotentials of Goedecker form [42]. The ions are kept frozen at the ground state structure, which is legitimate for the short time scales considered here.

Electron dynamics is described by TDDFT at the level of the Time-Dependent Local-Density Approximation (TDLDA) propagated directly in the time domain and using the xc -functional of [43]. The LDA is augmented by a self-interaction correction [44]. This is crucial to achieve a relevant dynamical picture of emission properties. In practice, we use an average-density self-interaction correction [45]. This formalism is simple and yet reliable for a broad variety of molecules including covalently bound systems [46]. To analyze observables from electronic emission, we apply absorbing boundary conditions following [40, 47].

A word is in order about the limits of TDLDA in the dynamics of strong photon excitations. A mean-field description cannot account for dynamical correlations by electron-electron collisions. These convert incoming energy into intrinsic heat which is released with large delay by thermal electron emission. Thus, TDLDA does not account at all for thermal electron emission and overestimates direct electron emission. However, experiments collect all electrons emitted from a cluster without discriminating arrival times, thus also including thermal electrons. This has to be kept in mind in the comparison with data later on. Thermal effects are so far mainly described phenomenologically, see e.g. [19]. A detailed account of collisional thermalization is presently only possible in semi-classical models of clusters dynamics [48, 49], which, however, work so far only in metal clusters. A quantum-mechanical modeling of thermalization has been proposed recently [50] which is, however, still too elaborate to be used for a large system as C_{60} . One should finally mention that, on top of electronic thermal effects, the impact of ionic temperature should

be added. Experimentally speaking, C_{60} are produced at finite temperature, typically several hundreds of K, which implies sizeable temperature effects at the side of ions. This is in principle not a problem for TDDFT which can perfectly accommodate an ionic temperature in the course of the dynamics and ideally lead to a description in terms of an ensemble of TDDFT evolutions. Still, because C_{60} is a large object, a proper description in terms of an ensemble of TDDFT computations remains extremely demanding in terms of computational cost. We shall thus recur to the zero temperature case all over the applications.

2.2. Numerical aspects

The numerical solution of the (time-dependent) Kohn-Sham equations for the cluster electrons proceeds with standard techniques as described in [40, 41]. The electronic wave functions and the spatial fields are represented on a Cartesian grid in three-dimensional coordinate space with grid spacing $0.71 a_0$ and total box size of $(112 \times 0.71 a_0)^3$. The absorbing boundary conditions are taken spherical with the use of a radially symmetric mask function, which is active only in the absorbing zone beyond $|\mathbf{r}| > R_1 = 33 a_0$. The mask switches gently from 1 at $|\mathbf{r}| = R_1$ to 0 at the edges of the box. The spatial derivatives are evaluated via fast Fourier transformation. The ground-state configurations were found by accelerated gradient iterations for the electronic wave functions [51]. The ionic ground state configuration is constructed from the known symmetries of C_{60} [11, 52, 53], while the ionic radius is optimized by minimizing the ground state energy. Dynamical propagation is done by the time-splitting method for the electronic wave functions [54].

2.3. Excitation and observables

Photon excitation of the cluster electrons is described by an external dipole field V_{ext} which reads :

$$V_{\text{ext}}(t) = E_0 \mathbf{e}_z \cdot \mathbf{r} \sin(\omega_{\text{las}} t) \sin^2(\pi t / T_{\text{pulse}}) \quad , \quad (1)$$

and which is active in the time interval $0 \leq t \leq T_{\text{pulse}}$. The pulse length T_{pulse} relates to the full width at half maximum (FWHM) in terms of laser intensity, $\text{FWHM} \simeq T_{\text{pulse}}/3$. We will use short femtosecond (fs) pulses with moderate intensity and propagate a while after the pulse is over, typically up to $t = 2T_{\text{pulse}}$, in order to collect most of the emitted electrons.

Three (experimentally measured) observables will be computed : spectral distribution of dipole strength, photo-electron spectra (PES), and photo-electron angular distribution (PAD), the latter sometimes combined as PES/PAD. The dipole strength is obtained by excitation of all occupied single particle wave functions with an instantaneous boost $\varphi_\alpha(t=0) \mapsto \exp(i\mathbf{p}_{\text{boost}} \cdot \mathbf{r})\varphi_\alpha(t=0)$ and subsequent spectral Fourier Transform (FT) analysis of the emerging dipole moment of the electronic density [40, 55]. The strength $\mathbf{p}_{\text{boost}}$ of the boost is chosen such that the system remains safely in the linear regime with very small ionization (typically 10^{-2}). PES and PAD are investigated in connection with a laser pulse (1) of finite length. PAD are computed from accumulating the amount of absorbed electrons in angular bins of the absorbing zone [38]. PES are obtained by storing the time evolution of the electronic wave functions at selected measuring points close to the absorbing bounds and finally Fourier transforming the collected signal [37, 56]. Combined PES/PAD are evaluated as PES, however, using a dense grid of measuring points to obtain a sufficient angular

resolution. As clusters are usually observed in gas phase, we practically deal with isotropic ensembles of cluster orientations. This requires orientation averaging over observables collected from different orientations. This procedure requires a specific methodology and dedicated calculations which were recently explored in Na clusters in a series of papers [35, 39]. The actual procedure used here will be outlined in section 5.1.

To better analyze the details of the ionization dynamics, we shall also complement the computation of the above observables by the (asymptotic) depletion of each Kohn-Sham occupied level. Since we use absorbing boundary conditions through a mask function, the norm of each Kohn-Sham orbital $\varphi_i(\mathbf{r}, t)$ decreases with time. We thus define the depletion of each state as $\sigma^{(i)} = 1 - \int d\mathbf{r} |\varphi_i(\mathbf{r}, t \rightarrow \infty)|^2$. It can be shown that the $\sigma^{(i)}$'s are directly connected to the PES and provide interesting details on the ionization mechanism [57].

3. Ground-state properties

The C_{60} cluster is distinguished by its highly symmetrical structure, often denoted as a fullerene [11]. The ionic configuration is illustrated in the left panel of Figure 1. The structure can be described as a truncated icosahedron [52, 58]. It consists of

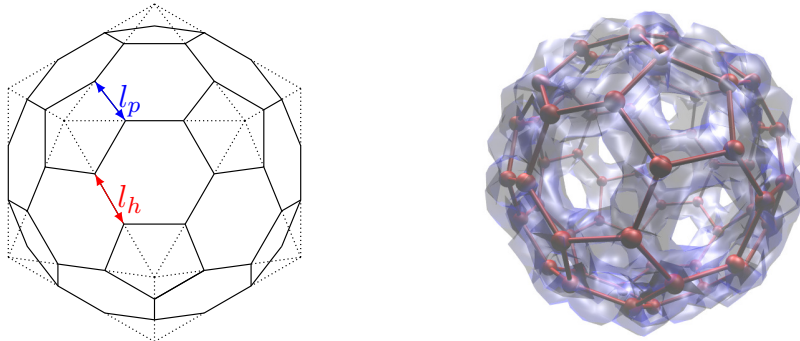


Figure 1. Left: Ionic structure of C_{60} with side lengths $l_h = 2.759 a_0$, $l_p = 2.915 a_0$, and radius $R_s = 6.763 a_0$. Right: Isosurface plot of the calculated electronic density.

20 hexagons and 12 pentagons. Each pentagon is surrounded by hexagons. The 12 pentagons constitute 6 pairs of opposite faces, the 20 hexagons constitute 10 pairs of opposite faces [53]. All atoms lie on a sphere of radius R_s . The icosahedron (= 20 regular triangles) is truncated in such a way that the resulting pentagons are regular with side length l_p and the hexagons are irregular with two side lengths l_p and l_h . After structure optimization within our DFT calculation, we get the values $l_h = 2.759 a_0$, $l_p = 2.915 a_0$, and $R_s = 6.763 a_0$. They are respectively 3-6% and 0.6% larger than the typical experimental values, that is, $l_h = 2.648 a_0$, $l_p = 2.755 a_0$, and $R_s = 6.721 a_0$ [58]. They can be considered as sufficiently close to each other for the present purpose.

The right panel of Figure 1 shows an isosurface plot of the calculated electronic density in C_{60} . This density concentrates well around the ions. It also follows predominantly the connecting lines, thus producing low-density region at the center of the hexagons and pentagons, and leaving a large void in the center of the cluster.

Although we have these pronounced low-density blobs, the electron channels are thoroughly connected, which suffices to deliver the typical metallic behavior of free electron flow throughout the whole cluster surface.

Figure 2 shows the spectrum of single-particle (s.p.) states. The occupied ones

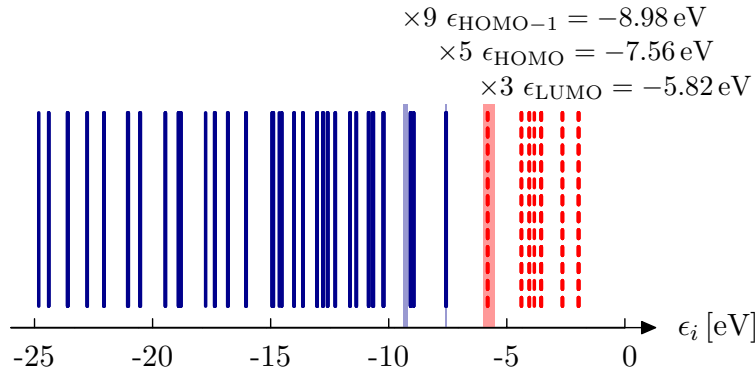


Figure 2. Calculated spectrum of single particle levels together with the degeneracy of HOMO, HOMO-1, and LUMO states. Experimental values of the LUMO [59], HOMO [12, 60, 61] and HOMO-1 [17, 59] are indicated as vertical shaded boxes.

are indicated by full lines and the first few unoccupied states by dashed lines. Spin-up and spin-down states are degenerated, thus leaving 120 occupied levels. The high symmetry of C_{60} leads to many degeneracies in the spectrum. We indicate in the figure the degree of degeneracy (without spin-degeneracy) for the most important states near the Fermi surface: the HOMO level is five-fold, the HOMO-1 nine-fold, and the LUMO triply degenerate. These degeneracies are also commonly obtained within Hückel molecular orbital theory when taking into account the icosahedral symmetry [62]. The HOMO-LUMO gap comes out at 1.74 eV in our calculations, in agreement with experimental values mostly within the range from 1.6 to 2.1 eV [59]. The energy difference from HOMO to HOMO-1 is of 1.42 eV, while experimental values are 1.6–1.8 eV [17, 59]. This is again a satisfying quality of reproduction in view of the complexity of C_{60} . The computed IP is 7.56 eV, which nicely agrees with the experimental value of 7.6 eV [12, 60, 61]. Note that a good reproduction of the IP is crucial for a proper description of photo-emission processes that we aim at here.

4. Optical response

Figure 3 shows the optical absorption (dipole) strength. Actually, this is the strength for excitation in z -direction (symmetry axis = axis through the center of a hexagon). The x - and y -modes are identical due to the high symmetry of the C_{60} cluster. Below the IP = 7.56 eV (left of the vertical arrow), the dipole response exhibits several discrete peaks. The lowest excitation energy of 4.1 eV is larger than the HOMO-LUMO gap. In the lower energy regime, there is one peak at 6.0 eV which dominates the other ones. It can be related to a collective resonance of the π electron system (π plasmon). Its position agrees well with other TDLDA calculations [65] and measurements [66, 67] (not shown on the figure to keep the very structured part below IP readable). Above the IP, the response is dominated by a broad Mie plasmon resonance around 19.2 eV.

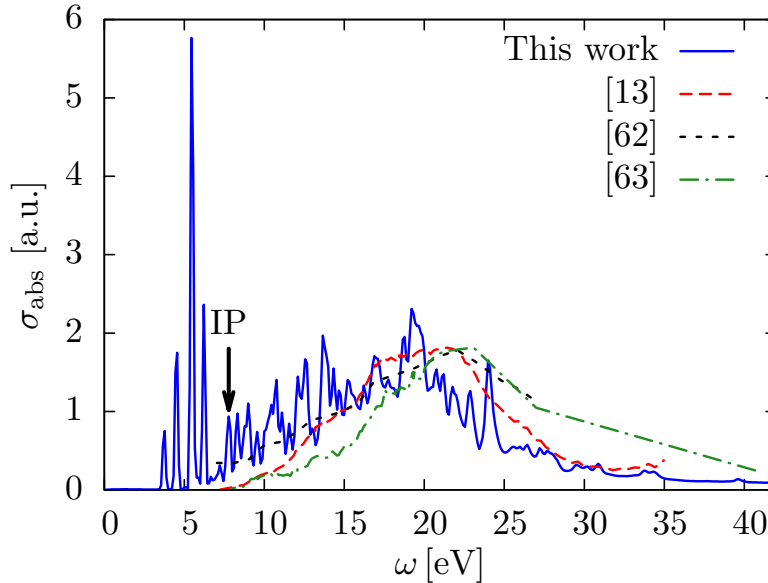


Figure 3. Calculated dipole strength distribution σ_{abs} of C_{60} (full line) for the mode in z -direction (vertical direction in the left panel of Figure 1), compared with experimental measurements [13, 63, 64]. The calculated ionization potential is indicated by the arrow.

It is much fragmented due to a coupling to the many one-particle-one-hole states in the vicinity of the resonance, a mechanism which is called Landau fragmentation, in analogy to Landau damping in a plasma [68]. This resonance is very broad with a fragmentation width (plus a sprinkle of continuum width) as large as 10 eV. Generally, the lower modes (below 14 eV) correspond to excitations of the highest occupied levels and have a $\pi-\pi^*$ character, while transitions from the σ subsystem also come into play at higher energies. The Mie plasmon resonance at 19.2 eV can be ascribed to a plasmon of all valence electrons ($\sigma+\pi$ plasmon). The experimental dipole strengths in Figure 3 show a smooth, broad plasmon peak centered in the same region, while the calculated distribution follows in the average the same trend but with larger fluctuations. This is a consequence of a mean-field description at fixed ionic configuration. Dynamical correlations beyond mean field lead to collisional broadening. Moreover, clusters are usually produced and measured at finite temperatures, e.g. at 300°C [63] or at 600°C [64, 66]. This induces thermal fluctuations of the cluster shape which, in turn, might also broaden the electronic excitations. Although thermal broadening is less dramatic in the rather rigid C_{60} cluster than in the much softer metal clusters [69], both broadening mechanisms together suffice to significantly smoothen the strength distribution [70].

5. Photo-emission in the one-photon regime

We now turn to situations where the free cluster is excited by photon pulses as they are usually provided at synchrotron facilities. In this section, we consider linearly polarized pulses with high frequencies ranging from 14 eV to 34 eV (which is far above the IP), but with weak intensities of about 10^{10} W/cm². In contrast to synchrotrons,

which deliver rather long pulses, we simulate the dynamics with short femtosecond (fs) pulses of length in the order of ~ 50 fs for reasons of computational cost. The photon excitation leads to a weak total ionization between 0.001 and 0.1. The dynamics thus safely stays in the perturbative regime with one-photon emission.

5.1. Orientation averaging scheme

Experiments are performed in gas phase on an ensemble of randomly oriented clusters. The isotropy of the ensemble simplifies the PAD. For mere one-photon processes, it takes the form

$$\frac{d\sigma}{d\cos\vartheta} = \frac{\sigma}{4\pi} [1 + \beta_2 P_2(\cos\vartheta)] , \quad (2)$$

where P_2 is the second Legendre polynomial, ϑ the (azimuthal) emission angle measured with respect to the photon polarization axis, σ the emission yield, and β_2 the anisotropy parameter. The PAD is symmetric under the following transformation $\vartheta \leftrightarrow \pi - \vartheta$, and independent of the polar angle φ . The anisotropy parameter β_2 can take values between $+2$ (pure \cos^2 -shaped emission aligned with the photon polarization) and -1 (pure \sin^2 -shaped emission perpendicular to the photon polarization).

In theory, the situation is different. Here, we calculate the PAD of a single cluster at fixed orientation. Hence, comparison of theory with experiment requires orientation averaging. An efficient scheme was developed in [35, 36, 71] which allows us to compute the orientation-averaged PAD (OA-PAD). We use here a direct averaging which can be done by discretizing the integral of PAD over the sphere of orientations over a large selection of reference points. Each cluster orientation can be represented by a rotation of a given initial ionic configuration about the three Euler angles α , β , and γ , as sketched in Figure 4. The final rotation (Euler angle α) about the photon polarization axis $\mathbf{e}_{\text{pol}} = \mathbf{e}_z$ does not require any additional TDLDA runs and can be done a posteriori by averaging the result over the polar angle φ of the laboratory frame. This leaves the Euler rotations $0 \leq \gamma < 2\pi$ about the z -axis and $0 \leq \beta < \pi$ about the y -axis. Both angles can be drawn on the unit sphere, see Figure 4 for a sample rotation. The corresponding orientation and sampling point are indicated by the red arrow and the red point, respectively. TDLDA calculations are then performed for each of these configurations, the obtained PAD are added (with proper weight factors), and finally averaged over the polar angle φ .

Although the direct averaging generally needs a lot of calculations for a sufficiently converged result, the high symmetry of C_{60} renders direct orientation averaging competitive with only five orientations. Figure 4 shows a set of 182 sampling points (only points in the foreground are displayed) superimposed by the icosahedral structure of C_{60} . For this particular chosen setting, the sampling points can be divided into 5 different groups of orientations which are connected by a symmetry operation. Indeed, it reduces the number of needed TDLDA calculations from 182 to 5 only.

Besides the calculation of the total OA-PAD of Eq. (2), the above procedure can, of course, also be used in order to calculate other orientation-averaged observables from emission such as the total ionization cross section σ , s.p. depletions $\sigma^{(i)}$, angular distributions of s.p. states $d\sigma^{(i)}/d\cos\vartheta$, photoelectron spectra $d\sigma/d\epsilon_{\text{kin}}$, and angle-resolved photoelectron spectra $d^2\sigma/(d\cos\vartheta d\epsilon_{\text{kin}})$. Results for each of these observables are presented in the following.

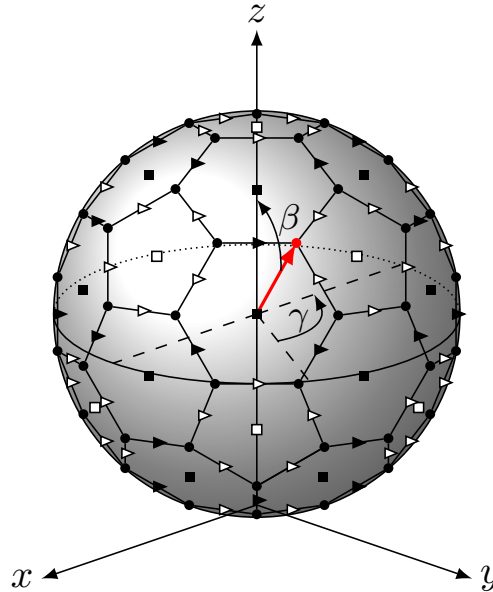


Figure 4. Illustration of the orientation averaging scheme. The Euler angles β and γ are shown for a sample cluster orientation (red arrow and red dot). For C_{60} , 182 well chosen points reduce to 5 different orientations indicated by dots, filled and unfilled triangles and squares (only points in the foreground are displayed).

5.2. A first illustrative example

Figure 5 shows one typical example for the full distribution $d^2\sigma/(d\epsilon_{\text{kin}} d\cos\vartheta)$ obtained in the mono-photon regime, visualized in a 3D projected map as the so-called Velocity Map Image (VMI). The map is drawn in polar coordinates where the angle ϑ stands for the emission angle with respect to the laser polarization, and the radial coordinate for the velocity $v_{\text{kin}} = \sqrt{2\epsilon_{\text{kin}}/m}$ of the emitted electron. One observes a series of rings, each one standing for one s.p. state. Moreover, one realizes that each ring has its own intensity (not necessarily isotropic) which means that different s.p. states can have different angular distributions [35].

Even if a VMI contains a priori richer information than PES or PAD separately, it is hard to extract quantitative information from such an image. We thus discuss in the following the full distribution integrated over ϑ , that is the PES, and the distribution integrated over ϵ_{kin} , that is the PAD. Figure 6 shows the PES and the OA-PAD for the same case as in Figure 5. The photon frequency is high enough to move all occupied states directly into the continuum by 1-photon absorption, and the laser intensity is low enough to produce a very low total ionization of 0.0078, such that dynamics stays in the linear regime. The lower panel shows the PES. When comparing the PES peaks with the s.p. levels as such (black vertical lines at the top of the lower panel), we have the impression that the PES somehow maps the s.p. spectrum. However, the different s.p. states obviously contribute with different weights to the PES. This weight is related to the depletion of the state by the photon pulse, which is a typically dynamical feature [57]. We thus weight the s.p. states with their actual depletion (recorded during the calculations) and give it a width corresponding to the resolution set by the finite width of the photon pulse. The result

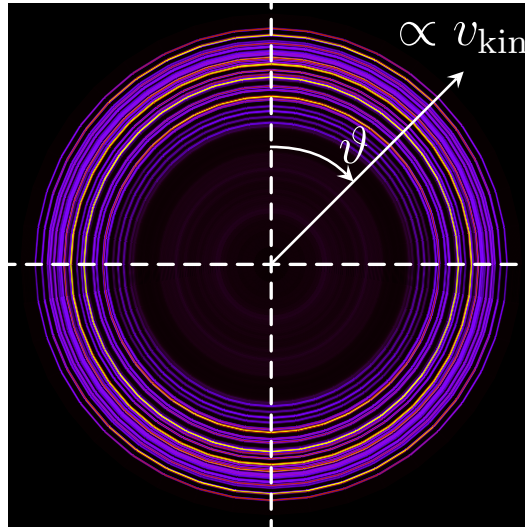


Figure 5. Velocity map image obtained for one-photon excitation of C_{60} with $\omega_{\text{las}} = 34 \text{ eV}$, $I = 10^{10} \text{ W/cm}^2$, and $T_{\text{pulse}} = 30 \text{ fs}$.

(denoted “depletion” in the figure) agrees perfectly with the explicitly computed PES. It demonstrates that measurement of PES gives indeed access to the spectra of the occupied states, however, weighted with the depletion. The latter strongly depends on the photon frequency [57], see discussion below.

As for the PAD in the top panel, the agreement of the computed OA-PAD with the second order polynomial Eq. (2) is almost perfect, delivering an anisotropy parameter of $\beta_2 = 0.41$. By a closer inspection, one can spot fluctuations about the smooth polynomial form. They stem from the finite resolution of the sampling of the angular bins, but they remain very small. This gives us confidence in our numerical scheme applied to such a demanding system.

5.3. Dependence on photon frequency

5.3.1. Photoelectron and depletion spectra We mentioned in connection with Figure 6 that the level depletion crucially depends on the photon frequency. In this section, we explore this effect. To this end, we use photon pulses with different frequencies, from 14 to 26 eV, and otherwise fixed parameters: pulse length of 60 fs and intensity of $7.8 \times 10^9 \text{ W/cm}^2$. Figure 7 shows PES (full lines) and level depletions (dashes) for four different photon frequencies around the Mie plasmon peak $\omega_{\text{Mie}} = 19.2 \text{ eV}$. The spectra dramatically change with ω_{las} , although the variation of frequency is not so large. Even if two-photon processes are in principle possible, they are much less likely than one-photon emission, especially at this low laser intensity. Indeed, the spectra vanish above $\omega_{\text{las}} - \text{IP}$ in each panel of Figure 7. However, even if the level sequences made accessible by one-photon processes remain the same throughout all frequencies, the s.p. depletions significantly change with frequency. One measurement alone may by chance mask this or that s.p. state. Ideally, one should thus measure PES at a couple of different and sufficiently high photon frequencies for a reliable extraction of

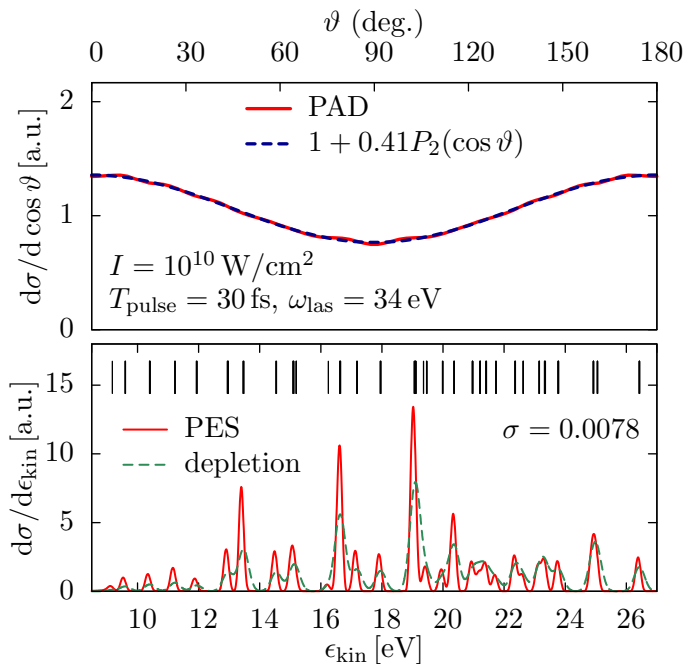


Figure 6. Orientation-averaged photoangular distribution (upper) and photoelectron spectrum (lower) obtained for one-photon excitation of C_{60} with $\omega_{\text{las}} = 34 \text{ eV}$, $I = 10^{10} \text{ W/cm}^2$, and $T_{\text{pulse}} = 30 \text{ fs}$, with total ionization of $\sigma = 0.0078$. The PAD is superimposed to the fit given in Eq. (2). The PES is superimposed to the single particle (s.p.) spectrum represented by Gaussians of constant width of 0.17 eV , weighted by the depletion of the s.p. states, and shifted by ω_{las} . The black vertical lines in the lower panel indicate the (shifted) positions of the s.p. states without weight.

s.p. spectra. The sudden drop of signal above the one-photon threshold $\omega_{\text{las}} - \text{IP}$ is particularly pronounced for weak photon pulses. More intense pulses can more easily access deeper levels. Still, the strong dependence of depletion spectra remains also for other intensities (not shown here). At the side of the PES, the correlation with the depletion spectra seems robust when the laser frequency varies. However the PES signal does not trivially provide a one-to-one reproduction of the s.p. density of state. It comes along overlaid with dynamical features as, e.g., level depletion and pulse profile.

5.3.2. Photoangular distributions We now turn to the frequency dependence of PAD. Figure 8 shows the PAD for different photon frequencies, total PAD and selective for the group of HOMO and HOMO-1 levels. Note that the latter states are those which are experimentally analyzed the best [72]. In a given panel, each curve corresponds to one frequency and the number in parentheses is the β_2 resulting from a fit according to Eq. (2). For total PAD (upper panel), the β_2 values do not change much with frequency and are comparable to the test case at $\omega_{\text{las}} = 34 \text{ eV}$ in Section 5.2. This shows that a global PAD only provides a gross measure of the dynamics. Much more sensitivity is seen for the PAD for HOMO (middle panel) and HOMO-1 (lower panel). Both s.p. anisotropies alone cover a larger range of values than the total β_2 . Even

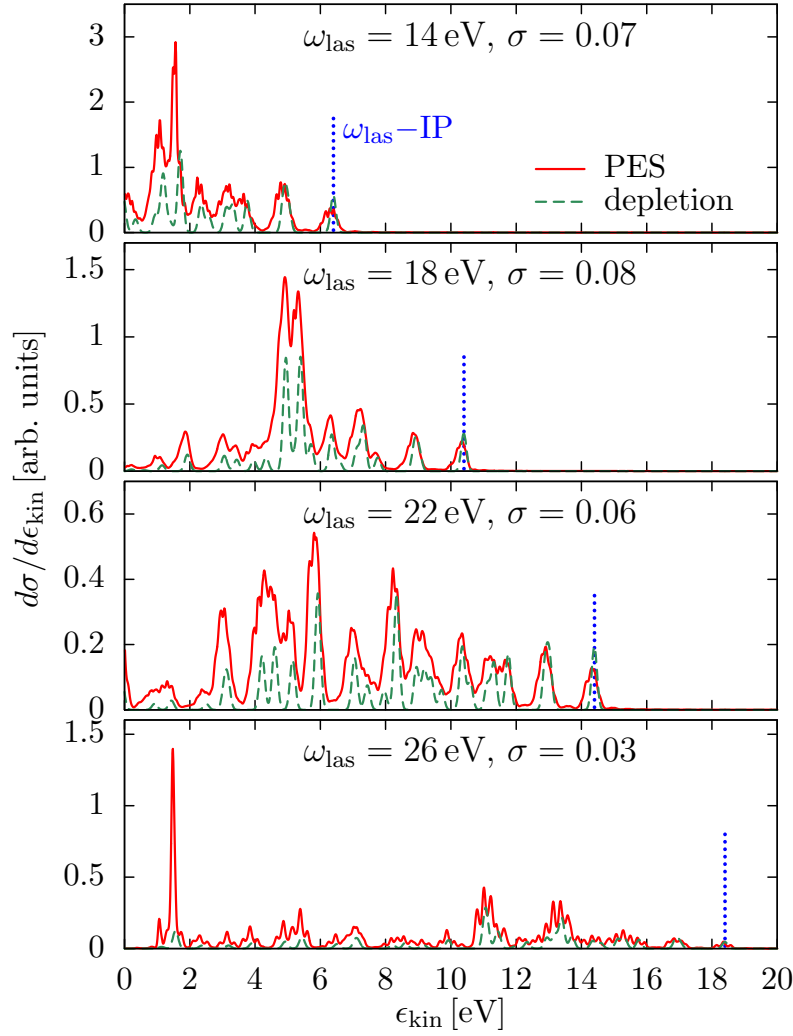


Figure 7. C_{60} after irradiation by a laser pulse of pulse length of 60 fs and intensity of 7.8×10^9 W/cm², and for different photon frequencies ω_{las} and corresponding total ionization σ as indicated : Photoelectron spectra (full lines) superimposed by single particle (s.p.) depletion spectra (dashes) with a folding with Gaussians of constant width of 0.08 eV, as is done in the bottom panel of Fig. 6. The dotted blue vertical lines indicate the threshold $\omega_{\text{las}} - \text{IP}$ for one-photon ionization (= ionization from the HOMO level).

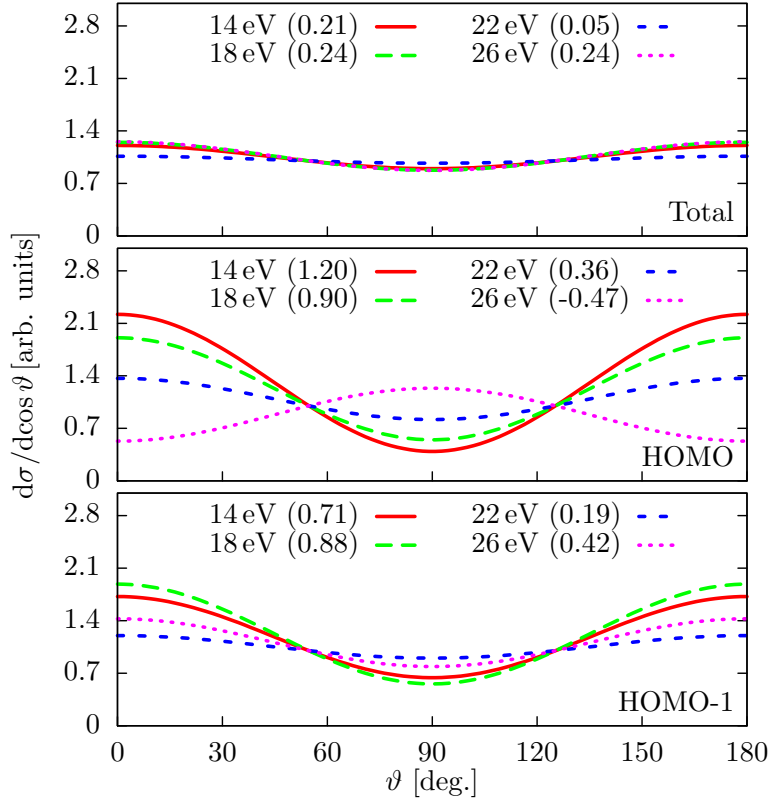


Figure 8. PAD of all s.p. states (top), HOMO (middle), and HOMO-1 (bottom) after irradiation by a laser with $I = 7.8 \times 10^9 \text{ W/cm}^2$, $T_{\text{pulse}} = 60 \text{ fs}$, and different photon frequencies as indicated. Corresponding values for the anisotropy parameter β_2 are given in brackets.

negative values (corresponding to emission preferably perpendicular to the photon polarization) appear for the HOMO level at 26 eV. These larger variations of the s.p. anisotropies seem to be washed out when added up into the total anisotropy. State-resolved PAD, on the other hand, are much more sensitive to details of the system and dynamics. They show sizeable variations from one level to the next and they depend significantly on the laser frequency, a feature which we had already observed for the PES.

Figure 8 indicates that the PAD of HOMO and HOMO-1 vary significantly when going through the resonance energy, while the total PAD remains robust. Figure 9 analyzes that in terms of single particle β_2 on a denser mesh of frequencies ω_{las} around the plasmon region $\omega_{\text{Mie}} = 19.2 \text{ eV}$. It confirms these trends. Mind, however, that theoretical spectra in the plasmon region, located above the IP, are fragmented into closely packed sub-peaks, see Figure 3. Each single peak may produce resonant ionisation effects and significantly affect the PAD. The situation is different in experiments where, in particular, ionic temperature will lead to a smoothing of the optical peaks into one broad and smooth structure around 20 eV. This may soften quick variations of the PAD signal with laser frequency and lead to a smoother behaviour altogether. Still, the comparison with previous experimental measurements [20] is

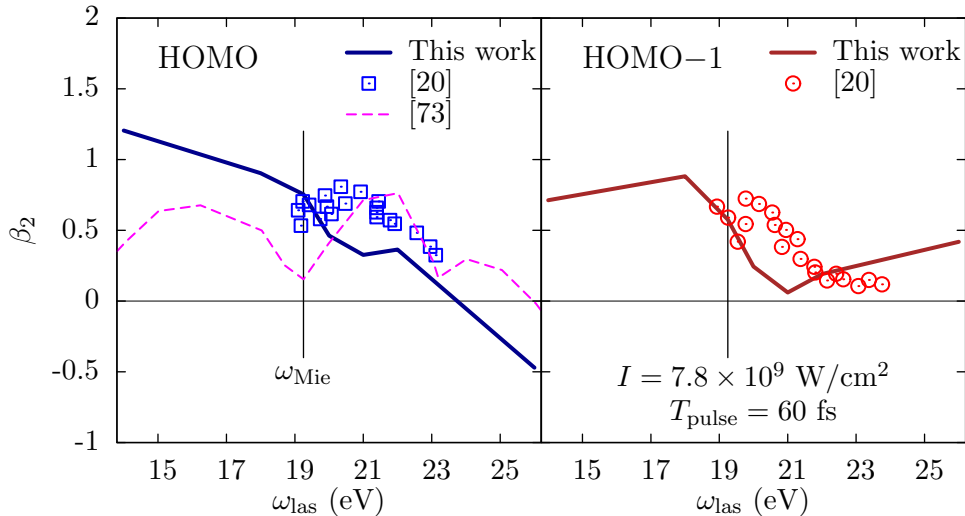


Figure 9. Anisotropy parameters β_2 as a function of ω_{las} , from the HOMO (left panel), and from the HOMO-1 (right panel), with a comparison of calculated values from this work (full lines) with experimental ones (symbols) [20], and with another theoretical work for the HOMO only (dashed line) [73]. The vertical line indicates the position of the calculated Mie plasmon frequency.

fairly good, especially around ω_{Mie} . The direct plotting of β_2 makes it also clearly visible that the total β_2 is far from any average between that of HOMO and that of HOMO-1. There are indeed many more states contributing substantially to the total β_2 as can read off from the right panels of Figure 7.

To conclude this discussion, we also compare our obtained β_2 for the HOMO state with another calculation from [73], see dashed curve in the left panel of Figure 9. These theoretical results are based on static calculations of matrix elements of the dipole operator at the level of Hartree-Fock molecular orbitals and the resolution of scattering equations by the single-center-expansion method. The discrepancies with our calculations are large. However, they also significantly differ from the experimental β_2 . This demonstrates that β_2 is an extremely sensitive observable at the side of the theory. And indeed, we have recently shown that ionization cross-sections and anisotropy parameters strongly change when one uses as outgoing wave functions either free plane waves, waves confined in a square well or waves self-consistently calculated in a Kohn-Sham picture [29].

6. An excursion into the multiphoton regime

Thus far, we have discussed one-photon processes using VUV pulses. At lower laser frequencies, multi-photon ionization (MPI) is the way to electron emission. We consider here the example of an infrared laser with $\omega_{\text{las}} = 1.55 \text{ eV}$ for which many experiments have been done. The laser intensity has to be higher to achieve an electron yield comparable with the monophoton case. The top panel of Figure 10 shows the calculated PES (full line) compared with three different experiments of about similar laser parameters. The theoretical curve shows a clear peak structure

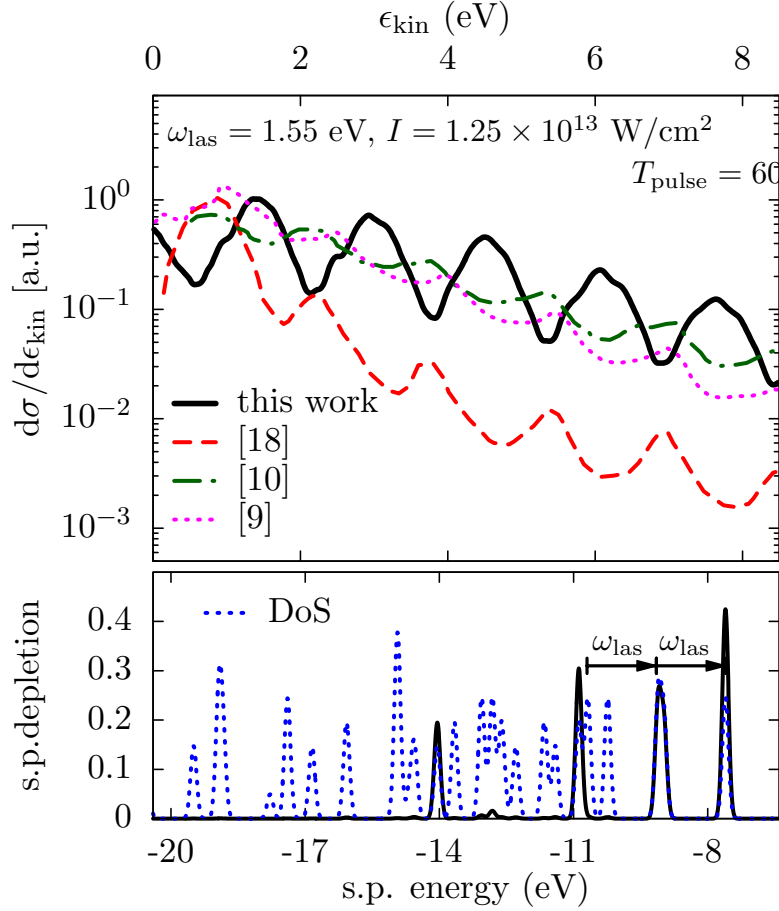


Figure 10. Top : calculated photoelectron spectrum (full line) with $I = 1.25 \times 10^{13}$ w/cm², $\omega_{\text{las}} = 1.55$ eV, $T_{\text{pulse}} = 60$ fs and compared with experimental measurements. Dashes : $I = (8 \pm 2) \times 10^{13}$ w/cm², $\omega_{\text{las}} = 1.57$ eV, FWHM= 25 fs [18] ; Dots and dashes : $I = 10^{13}$ w/cm², $\omega_{\text{las}} = 1.55$ eV, FWHM= 60 fs [10] ; Dots : $I = 2 \times 10^{13}$ w/cm², $\omega_{\text{las}} = 1.55$ eV, $T_{\text{pulse}} = 60$ fs [9]. Bottom : calculated depletion (solid line) of single particle states, compared with a (static) density-of-states (DoS) from all orbitals (dots).

with peak distance of ω_{las} and nearly exponential decrease of the envelope. The exponential envelope is a known feature of MPI [74]. The surprise is here rather that we see such well developed peaks in distances of 1.55 eV in spite of the fact that the s.p. spectrum is spread densely over 17 eV $\gg \omega_{\text{las}}$. The explanation is found in the lower panel of Figure 10. The actual depletion (full line) addresses only a few states near the HOMO while the rest of the spectrum (see dotted line “DoS”) remains untouched. Moreover, these few states happen to line up fairly well with ω_{las} . Thus the various multi-photon processes accumulate to the same peak positions in the PES. For example, the first peak at 1.4 eV is composed from a process with 6 photons from the HOMO, 7 photons from HOMO−1, and 8 photons from the HOMO−3 group. The alignment of frequencies is not perfect due to a slight mismatch of the HOMO−3. This leads to faint kinks in the theoretical peaks of the PES. Moreover, simple photon

counting would predict the first peak in the PES to appear at 1.7 eV. Actually, it is seen here at 1.4 eV. This downshift, called Coulomb shift, is an effect from ionization during emission. The total ionization is here about 0.06. The thus higher charge state enhances the Coulomb field of the cluster which, in turn, shifts all s.p. energies to slightly deeper binding [37].

The experimental PES are all recorded with slightly different laser parameters. Nonetheless, experimental and theoretical results show all in a similar fashion this typical regular sequence of peaks with exponentially decreasing envelope. This indicates that the same MPI mechanism is at work where only few levels near the HOMO contribute whose energy difference matches approximately ω_{las} . Going into quantitative detail, we have to compare the key features of these PES: peak positions, peak spacings, exponential slope, and amplitude of the peaks. Peak spacings are the same for the four cases, but the three other key features differ. This is not surprising as the conditions are not exactly the same. But the differences demonstrate how extremely sensitive PES depend on the dynamical conditions.

For instance, the peak positions signal the ionization stage which crucially depends on the IP, the actual laser intensity and the temporal pulse profile. However, neither the laser intensity nor the pulse duration are precisely known experimentally, while these two parameters strongly influence the final ionization stage and thus the Coulomb shift. This is particularly visible when comparing the dotted [72] and the dashed-dotted [10] PES for which the laser intensities differ by 25 %, and the pulse duration maybe by a factor of 3. Therefore, even if the laser parameters are very close in both experiments, the PES are almost out of phase. The slope of the PES background also depends on the field strength (thus intensity) : the higher the laser intensity, the smaller the slope [74]. However, if we take the experimental values of the laser intensity as such, we observe the reverse since the largest intensity delivers the largest slope. Therefore this uncertainty on the laser intensities in an experiment once again hinders a quantitative comparison with the theory. Note nevertheless a fair agreement of the theoretical slope with the experimental one from [10] since in both cases, one gets the same slope with a slight increase of the slope above $\epsilon_{\text{kin}} \simeq 5$ eV.

Finally, the amplitude of the peaks is particularly involved, being composed from broadening by Coulomb shift [37] and electron thermalization. It is worth mentioning that in [9], a theoretical PES calculated within TDLDA but in the jellium approximation is compared to an experimental PES using the same setup of [72] but at a slightly higher intensity ($I = 2 \times 10^{13}$ W/cm²) and measured at 90° with respect to the laser polarization. The positions of the peaks were satisfactory but the contrast of the MPI peaks was overestimated by the theoretical calculations by more than two orders of magnitude. Here, we also get too large a peak contrast in the theoretical curve but the discrepancy is less than a factor 10. This means that explicit ions surely bring more dissipative effects at the side of electron-ion collisions, and thus dramatically reduce the amplitude of the peak oscillations. Now, it is still too large when compared with the experimental ones. Two complementing effects can explain this difference. The missing of electron-electron collisions at TDLDA level generally produces a larger amplitude. This is in particular an important effect at low ϵ_{kin} . Moreover, we should emphasize that if the calculations are done at 0 K, this is far from being the case in the experiments, in which the temperature of the C_{60} jet ranges from 700 K to 850 K [10, 18, 72]. And we know that a finite ionic temperature tends to blur high electron energy peaks and thus reduces signal to background contrast [72].

We end up this discussion with Figure 11 which shows a combined PES/PAD,

this time plotted in a rectangular plane of energy and angle. Remind that the first

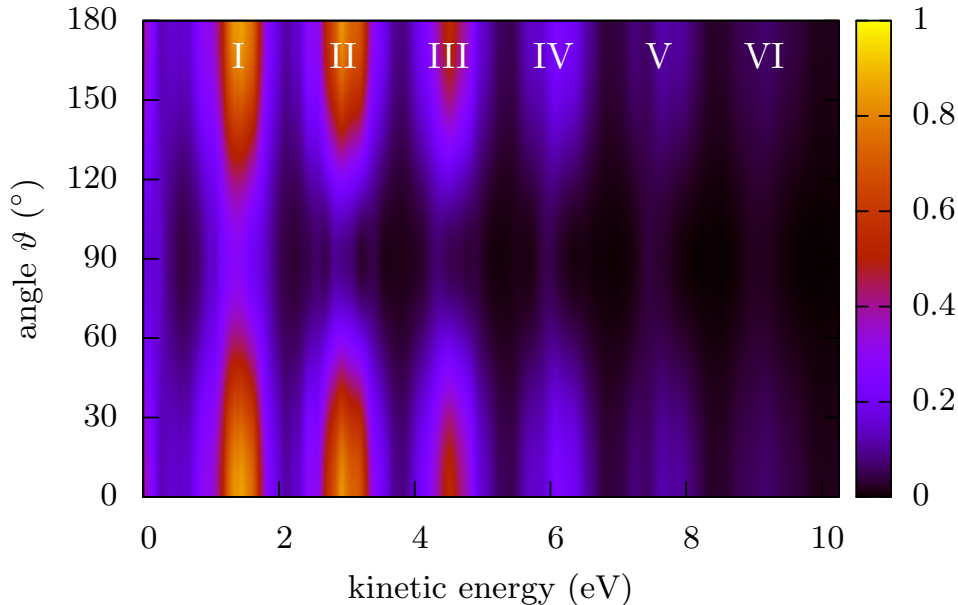


Figure 11. Theoretical combined PES/PAD in the same multiphoton regime as in Figure 10, that is $I = 1.25 \times 10^{13}$ W/cm², $\omega_{\text{las}} = 1.55$ eV, $T_{\text{pulse}} = 60$ fs. Each peak is labeled by a roman letter (see text for details).

peak appearing in this plot corresponds to a 6-7-8 photon process. Each further peak has one-photon-order higher. We see again the sequence of peaks as in Figure 10, which for completeness are identified with a roman number on the figure. New is the information on the angular distribution for each peak, which obviously depends on photon order. This is qualitatively clear from the figure but it can be made more quantitative by considering the β_2 values associated to each peak: they are evaluated to be respectively $\beta_2 = 0.77$ for peak I, $\beta_2 = 1.48$ for II, $\beta_2 = 1.50$ for III, $\beta_2 = 1.20$ for IV, $\beta_2 = 0.94$ for V and $\beta_2 = 0.92$ for VI. We thus roughly observe an increasingly forward emission as the number of involved photons increases. This feature agrees well with available experimental data [75]. Mind, however, that these β_2 are associated to rather large error bars of order of 0.5, and even 0.8 for the two highest energy peaks (V and VI) since they gather only little signal. Thus the levelling off of β_2 for point IV to VI should not be taken too serious. Moreover, a thorough analysis of PAD in the MPI regime would require to look at higher order Legendre polynomials in the expansion (2). This goes beyond the scope of the present paper. Still, the important point is that the β_2 exhibits a sizeable dependence on the photon order, which once again shows how sensitive this quantity is.

7. Conclusions

In this paper, we have investigated from a theoretical perspective ionization properties of C_{60} irradiated by lasers of various characteristics. To that end, we have used a fully microscopic description of electron dynamics based on time-dependent

density-functional theory (TDDFT) coupled to the (frozen) ionic background via pseudopotentials. We have checked that this setup delivers a good reproduction of ground state and low energy (optical response) properties of C_{60} . We have then explored ionization properties for the case of laser irradiations, considering the mono-photon regime as well as multi-photon processes. Thereby we concentrated particularly on energy- and angular-resolved emission cross-sections in terms of photo-electron spectra (PES) and photo-electron angular distributions (PAD). As experiments are usually done with C_{60} in gas phase, we perform an orientation averaging on all ionization properties to simulate the isotropic ensemble of orientations in the gas phase.

We have seen that both PES and PAD give access to structural properties of the cluster, however combined with dynamical features of the actual dynamical scenario. In the mono-photon regime, PES are expected to map the density of electronic states. In practice, this signal is folded with the depletion of each state and spectral profile of the laser. The case of C_{60} is a priori particularly involved regarding its complex s.p. spectrum. However, in every case studied in this paper, the PES peak positions and heights nicely correlate with the s.p. depletions. We also observe that increasing the laser frequency allows one to extract electrons from deeper and deeper states but not in a monotonous way. The symmetry of the orbitals certainly plays a role in the photoemission mechanism. The structure of PAD becomes very simple in the mono-photon regime, reducing information to only one number, the anisotropy β_2 . Nonetheless, PAD are found to provide worthwhile complementing information when considering their trends, e.g., as energy-resolved PAD or in dependence of systematically varied laser frequency. Here we find that the total anisotropy β_2 takes moderate values varying only slowly with frequency, while the β_2 for HOMO and HOMO-1 separately span a larger range of values and are highly sensitive to laser frequency, particularly around resonances. This is consistent with the fact that many states participate to the photoemission, and thus to the total β_2 , and not only the least bound states.

In the multi-photon regime, PES and PAD carry again combined information on cluster structure and dynamics of the excitation process, here with a stronger bias to dynamical influences. A major difference to mono-photon processes is that emission is concentrated to a few shells near the Fermi surface. As a consequence, PES are very structured with a sequence of peaks separated by the photon energy. A particularly clean structure is found if the photon energy matches the energy distances between HOMO, HOMO-1, and HOMO-3 shells. This result is in good agreement with measurements. Energy-resolved PAD nicely show that emission becomes increasingly forward focused with increasing number of photons involved.

The present survey was performed at zero temperature and ignored dynamical correlations from electron-electron collisions. Both effects tend to smooth spectral distributions, PES and PAD. They need to be included for a detailed reproduction of data. Work in that direction is in progress.

Acknowledgments

This work was supported by the Institut Universitaire de France. C.Z.G. receives financial support from China Scholarship Council (CSC) (No. [2013]3009). This work was granted access to the HPC resources of IDRIS under the allocation 2014-095115 made by GENCI (Grand Equipement National de Calcul Intensif), of CalMiP

(Calcul en Midi-Pyrénées) under the allocation P1238, and of RRZE (Regionales Rechenzentrum Erlangen).

- [1] de Heer W A 1993 *Rev. Mod. Phys.* **65** 611
- [2] Brack M 1993 *Rev. Mod. Phys.* **65** 677–732
- [3] Kreibig U and Vollmer M 1993 *Optical Properties of Metal Clusters* vol 25 (Springer Series in Materials Science)
- [4] Haberland H (ed) 1994 *Clusters of Atoms and Molecules 1- Theory, Experiment, and Clusters of Atoms* vol 52 (Berlin: Springer Series in Chemical Physics)
- [5] Haberland H (ed) 1994 *Clusters of Atoms and Molecules 2- Solvation and Chemistry of Free Clusters, and Embedded, Supported and Compressed Clusters* vol 56 (Berlin: Springer Series in Chemical Physics)
- [6] Gosh P 1983 *Introduction to photoelectron spectroscopy* (New York: Wiley)
- [7] Cooper J and Zare R N 1969 Photoelectron angular distribution *Lectures in Theoretical Physics: Atom Collision Processes* vol 11 ed Geltman S, Mahanthappa K and Brittin W (Gordon and Breach, New York)
- [8] Eppink A T J B and Parker D H 1997 *Rev. Sci. Instrum.* **68**
- [9] Huismans Y, Cormier E, Cauchy C, Hervieux P A, Gademann G, Gijsbertsen A, Ghafur O, Johnsson P, Logman P, Barillot T, Bordas C, Lépine F and Vrakking M J J 2013 *Phys. Rev. A* **88**(1) 013201
- [10] Fennel T, Meiwes-Broer K H, Tiggesbäumker J, Reinhard P G, Dinh P M and Suraud E 2010 *Rev. Mod. Phys.* **82** 1793
- [11] Kroto H W, Heath J R, O'Brien S C, Curl R F and Smalley R E 1985 *Nature* **318** 162–163
- [12] de Vries J, Steger H, Kamke B, Menzel C, Weisser B, Kamke W and Hertel I V 1992 *Chem. Phys. Lett.* **188** 159
- [13] Hertel I V, Steger H, de Vries J, Weisser B, Menzel C, Kamke B and Kamke W 1992 *Phys. Rev. Lett.* **68** 784
- [14] Kroto H 1997 *Rev. Mod. Phys.* **69** 703
- [15] Lichtenberger D L, Nebesny K W and Ray C D 1991 *Chem. Phys. Lett.* **176**
- [16] Benning P J, Poirier D M, Troullier N, Martins J L, Weaver J H, Haufler R E, Chibante L P F and Smalley R E 1991 *Phys. Rev. B* **44**(4) 1962–1965
- [17] Liebsch T, Plotzke O, Heiser F, Hergenbühn U, Hemmers O, Wehlitz R, Viehhaus J, Langer B, Whitfield S B and Becker U 1995 *Phys. Rev. A* **52** 457
- [18] Campbell E E B, Hansen K, Hoffmann K, Korn G, Tchapyguine M, Wittmann M and Hertel I V 2000 *Phys. Rev. Lett.* **84** 2128
- [19] Hansen K, Hoffmann K and Campbell E E B 2003 *J. Chem. Phys.* **119** 2513
- [20] Korica S, Rolles D, Reinköster A, Langer B, Viehhaus J, Cvejanović S and Becker U 2005 *Phys. Rev. A* **71** 013203
- [21] Maurat E, Hervieux P A and Lépine F 2009 *J. Phys. B: At. Mol. Opt. Phys.* **42** 165105
- [22] Kjellberg M, Johansson O, Jonsson F, Bulgakov A V, Bordas C, Campbell E E B and Hansen K 2010 *Phys. Rev. A* **81** 023202
- [23] Johansson J O, Henderson G G, Remele F and Campbell E E B 2012 *Phys. Rev. Lett.* **108** 173401
- [24] Troullier N and Martins J L 1992 *Phys. Rev. B* **46** 1754
- [25] Yabana K and Bertsch G F 1996 *Phys. Rev. B* **54**(7) 4484–4487
- [26] Korica S, Reinköster A, Braune M, Viehhaus J, Rolles D, Langer B, Fronzoni G, Toffoli D, Stener M, Declava P, Al-Dossary O and Becker U 2010 *Surf. Sci.* **604** 1940–1944
- [27] Toffoli D and Declava P 2010 *Phys. Rev. A* **81** 061201(R)
- [28] Toffoli D, Stener M, Fronzoni G and Declava P 2011 *Chem. Phys. Lett.* **516** 154–157
- [29] Wopperer P, Reinhard P G and Suraud E 2013 *Ann. der Physik* **525** 309
- [30] Madjet M E, Chakraborty H S, Rost J M and Manson S T 2008 *J. Phys. B: At. Mol. Opt. Phys.* **41** 105101
- [31] McCune M A, Madjet M E and Chakraborty H S 2008 *J. Phys. B* **41** 201003
- [32] Verkhovtsev A, Korol A and Solov'yov A 2012 *Eur. J. Phys. D* **66** 253
- [33] Bolognesi P, Avaldi L, Ruocco A, Verkhovtsev A, Korol A and Solov'yov A 2012 *Eur. J. Phys. D* **66** 254
- [34] Verkhovtsev A, Korol A and Solov'yov A 2013 *J. Phys. : Conf. Ser.* **438** 012011
- [35] Wopperer P, Faber B, Dinh P M, Reinhard P G and Suraud E 2010 *Phys. Lett. A* **375** 39
- [36] Wopperer P, Faber B, Dinh P M, Reinhard P G and Suraud E 2010 *Phys. Rev. A* **82** 063416
- [37] Pohl A, Reinhard P G and Suraud E 2000 *Phys. Rev. Lett.* **84**
- [38] Pohl A, Reinhard P G and Suraud E 2004 *Phys. Rev. A* **70**
- [39] Wopperer P, Reinhard P G and Suraud E 2013 *Ann. Phys. (Berlin)* **525** 309–321

- [40] Calvayrac F, Reinhard P G, Suraud E and Ullrich C A 2000 *Phys. Rep.* **337** 493
- [41] Reinhard P G and Suraud E 2004 *Introduction to Cluster Dynamics* (Wiley-VCH Verlag, Weinheim)
- [42] Goedecker S, Teter M and Hutter J 1996 *Phys. Rev. B* **54** 1703
- [43] Perdew J P and Wang Y 1992 *Phys. Rev. B* **45**(23) 13244–13249
- [44] Perdew J P and Zunger A 1981 *Phys. Rev. B* **23** 5048
- [45] Legrand C, Suraud E and Reinhard P G 2002 *J. Phys. B: At. Mol. Opt. Phys.* **35** 1115
- [46] Klüpfel P, Dinh P M, Reinhard P G and Suraud E 2013 *Phys. Rev. A* **88** 052501
- [47] Reinhard P G, Stevenson P D, Almelid D, Maruhn J A and Strayer M R 2006 *Phys. Rev. E* **73** 036709
- [48] Doms A, Reinhard P G and Suraud E 1998 *Phys. Rev. Lett.* **81** 5524
- [49] Fennel T, Bertsch G F and Meiwes-Broer K H 2004 *Eur. Phys. J. D* **29** 367
- [50] Reinhard P G and Suraud E 2014 *subm. Phys. Rev. A* ArXiv:
- [51] Blum V, Lauritsch G, Maruhn J A and Reinhard P G 1992 *J. Comput. Phys.* **100** 364
- [52] David W I F, Ibberson R M, Matthewman J C, Prassides K, Dennis T J S, Hare J P, Kroto H W, Taylor R and Walton D R M 1991 *Nature* **353** 147
- [53] Friepertinger H 1997 *J. Chem. Inf. Comp. Sci.* **37** 535
- [54] Feit M D, jr J A F and Steiger A 1982 *J. Comput. Phys.* **47** 412
- [55] Calvayrac F, Reinhard P G and Suraud E 1997 *Ann. Phys. (N.Y.)* **255** 125
- [56] Dinh P M, Romaniello P, Reinhard P G and Suraud E 2013 *Phys. Rev. A* **87**(3) 032514
- [57] Vidal S, Wang Z P, Dinh P M, Reinhard P G and Suraud E 2010 *J. Phys. B: At. Mol. Opt. Phys.* **43** 165102
- [58] Hedberg K, Hedberg L, Bethune D S, Brown C A, Dorn H C, Johnson R D and de Vries M 1991 *Science* **254**
- [59] Sattler K 2010 *Handbook of Nanophysics: Clusters and Fullerenes* Handbook of Nanophysics (CRC Press)
- [60] Zimmerman J A, Eyler J R, Bach S B H and McElvany W 1991 *J. Chem. Phys.* **94** 3556
- [61] Lichtenberger D L, Jatcko M E, Nebesny K W, Ray C D, Huffman D R and Lamb L D 1991 *Mater. Res. Soc. Symp. Proc.* **206**
- [62] Haddon R C 1992 *Acc. Chem. Res.* **25** 127–133
- [63] Keller J W and Coplan M A 1992 *Chem. Phys. Lett.* **193** 89
- [64] Yoo R K, Ruscic B and Berkowitz J 1992 *J. Chem. Phys.* **96** 911
- [65] Yabana K and Bertsch G F 1999 *Intern. J. Quant. Chem.* **75** 55
- [66] Smith A L 1996 *J. Phys. B: At. Mol. Opt. Phys.* **29** 4975
- [67] Yasumatsu H, Kondow T, Kitagawa H, Tabayashi K and Shobatake K 1996 *J. Chem. Phys.* **104** 899–902
- [68] Lifschitz E M and Pitajewski L P 1981 *Physical Kinetics (Course of Theoretical Physics vol X)* (Oxford: Butterworth-Heinemann)
- [69] Montag B and Reinhard P G 1995 *Phys. Rev. B* **51** 14686
- [70] Ellert C, Schmidt M, Schmitt C, Reiners T and Haberland H 1995 *Phys. Rev. Lett.* **75**(9) 1731–1734
- [71] Wopperer P, Dinh P M, Suraud E and Reinhard P G 2012 *Phys. Rev. A* **85**(1) 015402
- [72] Wopperer P, Gao C Z, Barillot T, Cauchy C, Marciniak A, Despré V, Loriot V, Celep G, Bordas C, Lépine F, Suraud E and Reinhard P G 2014 Submitted
- [73] Gianturco F A and Lucchese R R *Phys. Rev. A* **64** 032706
- [74] Pohl A, Reinhard P G and Suraud E 2004 *J. Phys. B: At. Mol. Opt. Phys.* **37** 3301
- [75] Li H 2013 *Study on molecular photoionization in femtosecond laser field* Master's thesis Kansas State University Manhattan, U.S.A. URL <https://krex.k-state.edu/dspace/handle/2097/15913>